Environmental
Science
Nano

PAPER

View Article Online
View Journal | View Issue

Check for updates

Cite this: *Environ. Sci.: Nano*, 2019, **6**, 2863

Do graphene oxide nanostructured coatings mitigate bacterial adhesion?†

Karl Wuolo-Journey,‡[a] Sara BinAhmed, ‡[a]
Elise Linna[a] and Santiago Romero-Vargas Castrillón *[abc]

Given its potent biocidal properties, graphene oxide (GO) holds promise as a building block of antimicrobial surfaces, with numerous potential environmental applications. Nonetheless, the extent to which GO-based coatings decrease bacterial adhesion propensity, a necessary requirement of low-fouling surfaces, remains unclear. Here we use AFM-based single-cell force spectroscopy (SCFS) to show that coatings comprising GO nanosheets bonded to a hydrophilic polymer brush mitigate adhesion of *Pseudomonas fluorescens* cells. We demonstrate low-adhesion GO coatings by grafting poly(acrylic acid) (PAA) to polyethersulfone (PES) substrates *via* self-initiated UV polymerization, followed by edge-tethering of GO to the PAA chains through amine coupling. We characterize the chemistry and interfacial properties of the unmodified PES, PAA-modified (PES–PAA), and GO-modified (PES–GO) substrates using ATR-FTIR, Raman spectroscopy, contact angle goniometry, and AFM to confirm the presence of PAA and covalently bonded GO on the substrates. Using SCFS we show that peak adhesion force distributions for PES–PAA (with mean adhesion force $\bar{F}_{\text{Peak}} = -0.13$ nN) and PES–GO ($\bar{F}_{\text{Peak}} = -0.11$ nN) substrates are skewed towards weaker values compared to the PES control ($\bar{F}_{\text{Peak}} = -0.18$ nN). Our results show that weaker adhesion on PES–GO is due to a higher incidence of non-adhesive (repulsive) forces (45.9% compared to 22.2% over PES–PAA and 32.3% over PES), which result from steric repulsion afforded by the brush-like GO–PAA interface. Lastly, we show that attachment to the various substrates is due to interactions of proteinaceous adhesins whose force response is well described by the worm-like chain model of polymer elasticity.

Received 2nd May 2019,
Accepted 25th July 2019

DOI: 10.1039/c9en00499h

rsc.li/es-nano

Environmental significance

While surface functionalization with graphene oxide (GO) is effective in bacterial inactivation, the modification of interfacial properties due to the nanomaterial coating may in fact increase the bioadhesion (and biofouling) propensity of a substrate. GO is biocidal; is it also anti-adhesive? Here we address this question using AFM-based bacterial adhesion force measurements. We show that coatings displaying low-bioadhesion properties can be formed by binding GO nanosheets to a hydrophilic polymer brush. Our work indicates that the underlying polymer layer enables a brush-like GO coating, which mitigates bacterial adhesion through steric repulsive forces. Conformational disorder (afforded by the polymer brush) is thus an important design variable for environmental interfaces (membranes, sorbents) seeking to exploit the antimicrobial properties of GO.

1. Introduction

The discovery of graphenic nanomaterials (GNMs, such as graphene, graphene oxide and reduced graphene oxide)[1] in 2004 unleashed a scientific revolution due to their unique physical and chemical properties, leading to numerous potential applications in water treatment and wastewater reuse.[2] The high specific surface area (~2630 m^2 g^{-1})[3] and single-atom-thickness of GNMs could enable them as membrane materials[4–6] and adsorbents for the removal of water contaminants.[7] Moreover, the thermal properties displayed by graphene (*i.e.*, its ability to harvest sunlight and increase the local temperature above the boiling point of water[8]), and graphene's high electron mobility (up to 2 × 10^5 cm^2 V^{-1} s^{-1}),[3] could enable electrochemical and solar-driven water purification and disinfection.

The specific application addressed by the present work concerns graphene oxide (GO)-based biocidal coatings.[9,10] Given their wide-spectrum antimicrobial activity,[11–14] GO nanosheets are being explored as building blocks of

---

[a] *Department of Civil, Environmental, and Geo- Engineering, University of Minnesota, 500 Pillsbury Dr. SE, Minneapolis, MN 55455, USA. E-mail: Santiago@ed.ac.uk, sromerov@umn.edu; Tel: +44(0)131 651 3567*
[b] *Institute for Infrastructure and Environment, School of Engineering, The University of Edinburgh, William Rankine Building, Thomas Bayes Road, Edinburgh, EH9 3FG UK*
[c] *Institute for Materials and Processes, School of Engineering, The University of Edinburgh, Sanderson Building, Robert Stevenson Road, Edinburgh, EH9 3FB UK*

† Electronic supplementary information (ESI) available. See DOI: 10.1039/c9en00499h

‡ These authors contributed equally to this work.

antimicrobial surfaces, aiming to inactivate water-borne bacteria and mitigate biofilm formation. In recent studies, GO has been incorporated into the polymeric matrix of polyamide membranes,[15–18] or covalently bonded to membrane surfaces.[19,20] Nevertheless, the underlying mechanism of bacterial adhesion to GO-functionalized interfaces—the crucial first step of biofilm formation[21]—continues to be poorly understood. Moreover, recent studies have observed that GO functionalization of inorganic and polymeric substrates can increase their bio-adhesiveness.[22,23] The possible adverse modification of interfacial properties challenges the notion of GO films as anti-biofouling coatings. This question needs to be addressed since the effectiveness of GO as a biocidal nanomaterial will be compromised if it increases the adhesiveness of a given substrate *vis-à-vis* bacterial cells.

In a recent study,[22] we reported that the nanoscale morphology of GO coatings significantly influences bacterial adhesion, with edge-tethered GO showing weaker adhesion forces compared to immobilized layers of horizontally arranged GO nanosheets; spatial arrangement and conformational disorder of the GO building blocks thus seem essential to realize both biocidal activity and low adhesion propensity. Here, we investigate the extent to which GO coatings, comprising GO nanosheets edge-tethered to a polymer brush, are capable of mitigating bacterial adhesion. We surmise that the combination of hydrophilicity and conformational disorder afforded by the GO-functionalized polymer brush is essential to mitigate bioadhesion. To test this hypothesis, we use self-initiated UV polymerization of acrylic acid to graft poly(acrylic acid) (PAA) to polyethersulfone (PES) substrates, tethering GO nanosheets to the PAA chains. We then explore the interfacial properties of the GO coatings using atomic force microscopy (AFM)-based single-cell force spectroscopy,[24] whereby a single *Pseudomonas fluorescens* cell (a Gram-negative, biofilm-forming bacterium[25,26]) is immobilized on an AFM cantilever, enabling investigation of bacterial adhesion with nanoscale resolution. We show that microbial adhesion to GO-functionalized substrates is weakened compared to the GO-free control substrates. Consistent with our AFM results, bacterial deposition experiments show that GO-functionalized substrates mitigate adhesion under dynamic conditions. Characterization of the surface interfacial properties suggests that weaker adhesion on GO-modified substrates is a consequence of steric repulsive forces derived from the GO layer, edge-tethered to PAA brushes.

This paper is organized as follows. In section 2 we describe the substrate modification protocols, and the techniques employed to characterize interfacial properties. Results and discussion are given in section 3. We close with concluding remarks in section 4.

2. Materials and methods

GO functionalization

Substrates. All coatings investigated were formed on polyethersulfone (PES) substrates. To this end, commercially available PES ultrafiltration (UF) membranes were used (30 kDa molecular weight cutoff; Synder Filtration, Vacaville, USA). PES substrates were soaked in 50% glycerin solution and stored at 4 °C. Prior to use, substrates were rinsed with ultrapure (UP) water (18.2 MΩ cm, Barnstead, Thermo Fisher), soaked in 25 vol% aqueous isopropanol for 24 hours, and thoroughly rinsed again with UP water to remove residual preservatives.

Poly(acrylic acid) grafting. We used self-initiated UV graft polymerization to grow poly(acrylic acid) (PAA) on PES.[27–31] PAA chains were subsequently used to functionalize substrates with GO. A schematic diagram of the surface modification protocol is given in Fig. 1. An aqueous acrylic acid (AA) solution (10 vol%) was prepared from a 99% AA stock solution (Sigma Aldrich) with UP water. PES coupons (9 × 14 cm^2) were attached to PTFE frames with a holding volume of 112 mL. The PES substrates and the AA solution were brought to a glove box, from which oxygen had been purged to a concentration < 500 ppm. The solution and the substrates were left to equilibrate with the atmosphere inside the glove box for 15 minutes to lower the dissolved oxygen concentration in the AA monomer solution. Next, 10 vol% AA solution was poured over the PES (affixed to the PTFE frame) and allowed to soak the PES substrate. After 15 minutes, excess AA solution was removed, leaving a thin liquid film of AA monomer solution on the surface (Fig. 1 (a)). Ensuring that the monomer solution is cast as a thin film increases UV penetration depth, thus accelerating the polymerization kinetics on the substrate. Subsequently, the AA-soaked PES surface was irradiated with a UV lamp (Spectroline Model EF-160C) positioned ~2 cm above the substrate for times ranging from 10 to 60 seconds. After irradiation, the substrate was rinsed thoroughly and soaked in UP water for 24 hours to remove unreacted monomers. This step resulted in PAA-functionalized PES substrates (Fig. 1 (b)), which hereinafter we designate as PES–PAA.

Substrate functionalization with GO. Single-layer graphene oxide (GO) was purchased from Cheap Tubes (Grafton, VT, USA). Characterization by AC mode AFM revealed an average nanosheet thickness of 0.8 ± 0.1 nm, consistent with single sheets,[22] and sub-micron lateral dimensions (Fig. S1 (a) and (b)†) in agreement with the manufacturer's specifications (*i.e.*, 300–800 nm). A negative zeta potential was observed over the pH range ~1.5–9 for GO in aqueous dispersion (Fig. S1 (c)†) (consistent with previous work[32]), indicative of deprotonation of carboxylic acid groups in the nanosheet edges.[10] The oxygen content of GO was 35–45%, per the manufacturer's specifications. The Raman spectrum of GO nanosheets deposited on a silicon wafer (Fig. S1 (d)†) exhibited the D (~1350 cm^{-1}) and G (~1590 cm^{-1}) bands characteristic of GO.[33] Substrates were functionalized with 250 μg mL^{-1} GO dispersions prepared from 2 mg mL^{-1} stock dispersions, which were rendered colloidally stable through bath sonication for 24 hours. PES–PAA substrates were functionalized with GO by adapting the procedure developed by Perreault *et al.*,[19] which is based on amine coupling.[34] Carboxylic acid

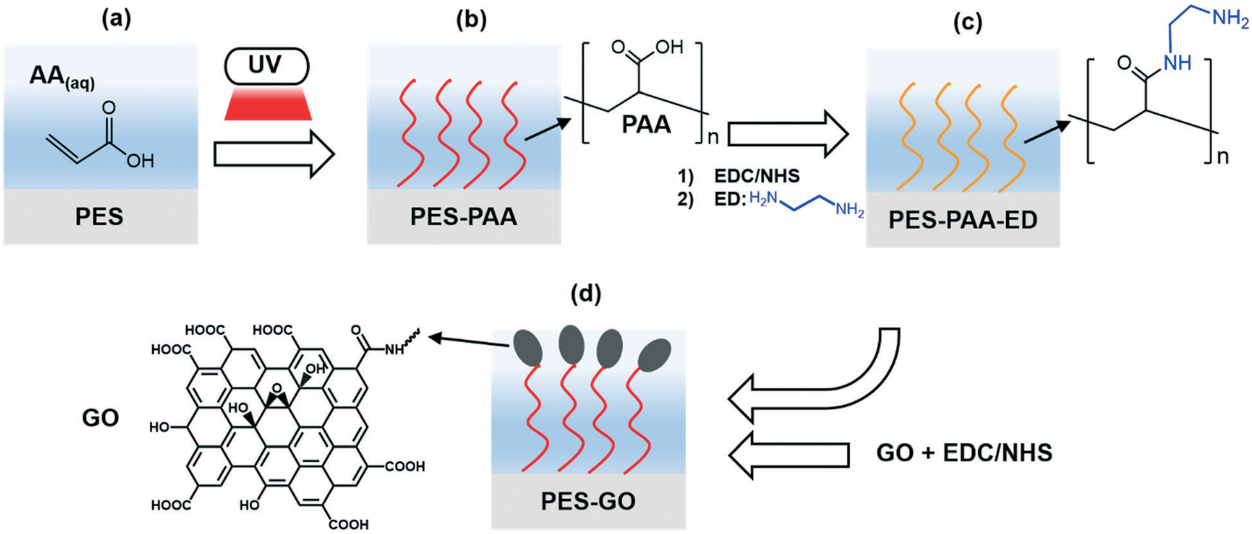

Fig. 1 Schematic diagram of polyethersulfone (PES) surface modification with graphene oxide (GO). (a and b) Self-initiated UV polymerization results in growth of poly(acrylic acid) (PAA) chains from acrylic acid (AA) monomers in aqueous solution, yielding PES–PAA substrates. (c) EDC/NHS-mediated amine coupling binds ethylenediamine (ED) linkers to the PAA chains, resulting in PES–PAA–ED substrates. (d) EDC/NHS-activated GO nanosheets react with primary amines in the ED linker to covalently tether GO to the substrates (yielding PES–GO substrates).

functional groups in the grafted PAA chains were activated to amine-reactive esters with 4 mM 1-ethyl-3-(3-dimethylaminopropyl)carbodiimide hydrochloride (EDC, 98%, Sigma) and 10 mM *N*-hydroxysuccinimide (NHS, 98%, Sigma), buffered at pH 5 with 10 mM MES (BioXtra, Sigma) supplemented with 0.5 M NaCl. The EDC–NHS activation step was carried out for 60 minutes under ambient conditions on a benchtop shaker at 30 rpm. Substrates were then rinsed gently with UP water. The amine reactive esters on the PES–PAA surface were subsequently contacted with 10 mM ethylenediamine solution (ED, BioXtra, Sigma) buffered at pH 7.5 by 10 mM HEPES (99.5%, Sigma) with 0.15 mM NaCl. The ED amine coupling step proceeded for 30 minutes, resulting in PES–PAA–ED substrates, as shown schematically in Fig. 1 (c). Next, the carboxylic acid functional groups decorating the GO nanosheet edges[10] were activated to amine reactive esters in a similar way. A GO dispersion (10 parts, 250 μg mL^{-1}) was mixed with 2 parts 100 mM MES buffer, followed by 1.75 parts 20 mM EDC in 10 mM MES buffer, and 1.75 parts 50 mM NHS in 10 mM MES buffer. The pH of the solution was then lowered to 5.5 by addition of 1 M HCl dropwise (to minimize flocculation of GO nanosheets), and allowed to react for 15 minutes. Subsequently, the pH was raised to 7.2 by addition of 1 M NaOH dropwise. The GO dispersion was poured over the ED-functionalized surface (PES–PAA–ED), covered, and allowed to react for 1 hour on a benchtop shaker at 30 rpm. Reaction between the amine-reactive esters in GO and the primary amine groups on the surface of the ED-modified substrate resulted in covalent linkage of the GO nanosheets to produce PES–GO substrates (Fig. 1 (d)). Finally, PES–GO samples were thoroughly rinsed and sonicated for 5 minutes to remove non-covalently bonded GO. All substrate samples were stored in ultrapure water at 4 °C for up to 3 weeks until use.

Interfacial characterization techniques

Raman and Fourier-transform infrared spectroscopy (FTIR). Attenuated total reflectance (ATR) FTIR was used to characterize the surface chemistry of the substrates. Spectra of desiccator-dried specimens of each substrate type were acquired in an FTIR spectrometer (Nicolet Series II Magna-IR System 750) equipped with an ATR cell. The spectra were collected in terms of % reflectance at a resolution of 0.241 cm^{-1}. Raman spectra were obtained with an Alpha300R Raman microscope (Witec). For each specimen, we acquired 20 × 20 μm^2 Raman scans at a 0.5 μm resolution, on randomly chosen sections of the substrates. At each point in the 2D scan, we computed the ratio of the area under the D band of GO (observed at 1350 cm^{-1})[33] and the area under a prominent PES peak (observed at 1146 cm^{-1}) to generate maps characterizing the spatial distribution of GO nanosheets. In addition, a mean Raman spectrum was generated by averaging the spectra collected at each point on the 2D scan.

Contact angle, surface charge, and nanoscale roughness. Substrate hydrophobicity was characterized in terms of oil-in-water contact angle measurements using the captive bubble technique. We performed measurements with a Ramé-Hart Model 200 goniometer; images were analyzed with the DROP Image software (Ramé-Hart). For captive bubble measurements, substrates were affixed to a surface with the functionalized side facing a liquid cell containing ultrapure water. A J-shaped needle was used to inject *n*-decane droplets (~10 μL). We performed ≥14 contact angle measurements across three independently functionalized specimens of each substrate type. The surface charge of the substrates was characterized *via* streaming potential measurements using an electrokinetic analyzer (SurPass, Anton-Paar) equipped with an adjustable gap cell at a gap size of 120 μm. Streaming potential was measured from pH 10 to pH 4 in 1 mM KCl solution, and the zeta potential was determined from the streaming potential using the Smoluchowski–Helmholtz equation.[35] Three specimens of each substrate type were characterized. The nanoscale roughness of the substrates was investigated with an MFP-3D-Bio AFM (Asylum Research) equipped with a liquid cell. AC mode AFM scans (5 × 5 μm^2, scan rate = 0.25 Hz) of two specimens of each substrate type were obtained in phosphate-buffered saline (PBS) at pH 7.4 using a silicon nitride cantilever (SNL probe "C", nominal k = 0.24 N m^{-1}, Bruker). Surface topography was quantified in terms of the root-mean-squared roughness (R_{RMS}) determined in 1 × 1 μm^2 areas of each of the AFM scans for a total of 8 roughness calculations for each substrate type.

Single-cell force spectroscopy (SCFS). The adhesion of *P. fluorescens* cells to the surface of control and functionalized substrates was quantitatively investigated using single-cell force spectroscopy (SCFS). Bacterial cells were grown and cultivated following the protocol provided in the ESI.† The experimental procedure of SCFS, outlined below, is provided in detail in our recent publication.[36] An individual *P. fluorescens* (ATCC 13525) cell was adhered to a tip-less AFM cantilever (MLCT-O10 probe "C", nominal k = 0.01 N m^{-1}, Bruker) on which a polydopamine wet adhesive layer had been deposited from a dopamine hydrochloride solution (4 mg of dopamine hydrochloride per milliliter of Trizma buffer, pH 8.5) shortly before adhering the cell. The cell was adhered with its long axis parallel to the leading edge of the cantilever, an orientation that maximizes adhesion contact area. Bacterium orientations probing adhesion *via* the flagellar pole were not studied, due to the risk of cell detachment during force collection. An MFP-3D-Bio AFM (Asylum Research) integrated to a Zeiss Axio Observer A1 inverted optical microscope was used to perform cell adhesion force measurements. All forces were determined at room temperature (25 °C) in a liquid cell filled with PBS, pH 7.4. Force curves, comprising extension–retraction cycles, were carried out at a cantilever speed of 400 nm s^{-1}, a piezo dynamic range of at least 3 μm, a trigger force (the maximum force applied to the cell as it contacts the substrate) of 600 pN, and a dwell time of 0 s (*i.e.*, the bacterial cell was immediately retracted from the substrate upon reaching the trigger force). For each substrate type, a total of ≥98 force curves were collected with at least 2 independently cultivated bacterial cells, on ≥2 different substrate specimens of each type. Force curves were acquired at randomly chosen sites on the substrate. At each randomly chosen location, up to three force curves were collected to minimize deposition of extracellular polymeric substances on the substrate. After each experiment, the cell viability was determined using a live/dead assay (BacLight, Thermofisher). Only data collected with a live cell that remained at its initial location were reported.

Statistical analysis. Unless stated otherwise, two-sided unpaired t-tests, presuming unknown but equal population variances (*i.e.*, assuming homoscedasticity), were conducted to determine the statistical significance of the results.

3. Results and discussion

Interfacial characterization

We used an array of surface analytical techniques to characterize the chemistry and morphology of the various substrates.

Surface chemistry. Given the prominent IR bands present in the AA monomer, we used FTIR spectroscopy to assess the efficacy of PAA grafting. AA polymerizes on the substrate due to UV-generated free radicals formed on the PES surface, which react with the vinyl double bond of the AA molecule, leading to the formation of PAA chains covalently bonded to the substrate.[29] The degree of grafting (*i.e.*, the extent of AA polymerization on the PES substrate), and the kinetics of polymerization, are influenced by the UV irradiation time and UV wavelength.[29,37] PES substrates soaked with a thin liquid film of 10 vol% AA solution were exposed to UV light for 10–60 seconds. The FTIR results for the PES control and PES–PAA substrates are shown in Fig. 2. The peak at 1580 cm^{-1}, observed in all samples, is due to vibration of the aromatic rings in PES.[38] In addition, we observe IR bands resulting from carboxylic acid groups in PAA, namely a peak at 1700–1730 cm^{-1} due to C=O stretching vibration,[39] and multiple bands in the 2500–3300 cm^{-1} range due to COO–H stretching.[39] These peaks increase monotonically with irradiation time, in line with increasing degree of PAA grafting.[37] In the remainder of the study we focus on substrates fabricated with a 10 s UV irradiation step, which resulted in materials with nanofiltration-like water permeability coefficient and divalent ion rejection (see ESI† for methods and results). Irradiation times > 10 s resulted in a dense PAA layer and a steep loss in water permeability.

The FTIR spectra of the PES, PES–PAA (10 s UV irradiation) and PES–GO substrates are presented in Fig. 3. The spectrum corresponding to PES–GO shows an increase in the COO–H stretching band at 3300 cm^{-1} relative to PES–PAA, which can be attributed to carboxylic acid functional groups present in the GO nanosheet edges.[10] In addition, PES–GO presents a peak at ~2900 cm^{-1} absent in the other substrates,

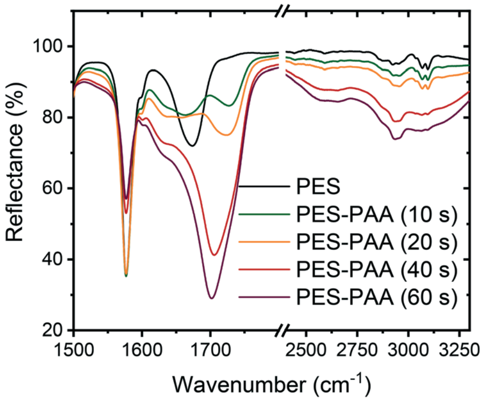

Fig. 2 FTIR spectra of PES and poly(acrylic acid) (PAA)-functionalized PES substrates (PES–PAA, prepared with different UV irradiation times noted in the caption).

which is likely an N–H stretching vibration band (typically observed at 3100–3500 cm^{-1} [39]) due to primary amines that remain unreacted after GO modification.

We confirmed the presence of graphene oxide on the PES–GO substrates using Raman spectroscopy. The average of 1600 spectra scanned over a 20 × 20 μm^2 area of each specimen is presented in Fig. 4. The PES–GO substrate prominently shows the G and D bands of graphene oxide,[33] thus confirming functionalization of PES with GO. All substrates show similar chemical signatures due to polyethersulfone, *e.g.*, peaks at 790, 1070, 1107, 1146, 1580 and 1601 cm^{-1}.[40]

We used confocal Raman mapping to assess the spatial distribution of GO on the PES–GO substrates. The results are presented in Fig. 5. The PES–GO map (Fig. 5 (c)) exhibits high brightness regions indicative of the presence of GO nanosheets throughout the scanned area (the intensity of each pixel is proportional to the ratio of the area under the D peak of GO to that under the polyethersulfone peak at 1146 cm^{-1}). Conversely, neither the PES nor the PES–PAA Raman maps (Fig. 5 (a and b)) exhibit signatures of GO. The data in Fig. 5 consequently show that the modification protocol enables the formation of uniform layers of tethered GO nanosheets on the PES substrates.

Interfacial properties. We investigated the interfacial properties which are known to influence biofouling propensity: hydrophobicity, nanoscale roughness and surface charge.[41,42] To characterize the hydrophobicity of each substrate type, we measured the contact angle of *n*-decane droplets in aqueous suspension using the captive bubble technique. The angles shown below are measured from the substrate, through the aqueous phase, to the *n*-decane interface, so that smaller values indicate poor wetting of the substrate by the *n*-decane droplet (*i.e.*, greater hydrophilicity). The results, presented in Fig. 6 (a), show that PES–PAA ($\theta_{n\text{-Decane}}$ = 20.6 ± 4.3°) and PES–GO samples ($\theta_{n\text{-Decane}}$ = 19.7 ± 5.4°) are significantly more hydrophilic ($p < 0.01$) than the control PES substrate ($\theta_{n\text{-Decane}}$ = 53.1 ± 3.9°). PES–PAA and PES–GO showed approximately equal contact angles ($p = 0.6$). We attribute the low wettability of PES–PAA and PES–GO surfaces by a hydrophobic liquid (*n*-decane) to the abundance of H-bonding functional groups in PAA- and GO-functionalized surfaces (*i.e.*, –COOH groups in PES–PAA; hydroxyl, and –COOH groups in GO,[10] all of which are absent in PES).

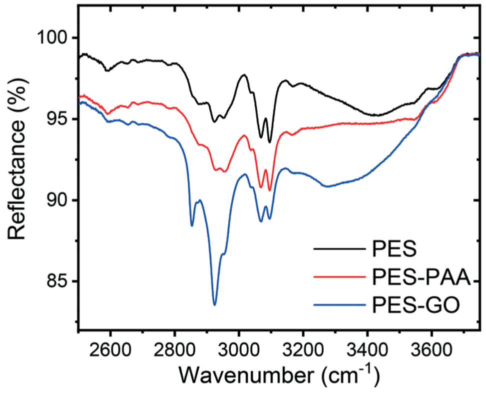

Fig. 3 FTIR spectra of control (PES), poly(acrylic acid) (PAA)-functionalized PES (PES–PAA, 10 s UV irradiation), and GO-functionalized (PES–GO) substrates.

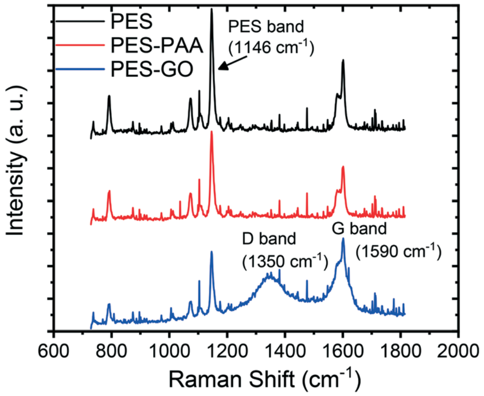

Fig. 4 Raman spectra of pristine PES, poly(acrylic acid) (PAA)-functionalized PES (PES–PAA), and GO-modified PES (PES–GO) substrates.

We characterized the surface charge of the substrates in terms of the ζ-potential as a function of pH. The results are presented in Fig. 6 (b). All substrates (including pristine PES[43]) exhibited negative zeta potentials over the pH range investigated. At pH 7.4, (*i.e.*, the condition at which we characterized other interfacial properties such as surface roughness, and microbial adhesion), all specimens show a similar zeta potential value of ∼−30 to −40 mV, suggesting that surface functionalization does not significantly modify the charge of the interface at this pH. PES–PAA and PES–GO samples are negatively charged primarily due to deprotonation of carboxylic acid groups with increasing pH.[10,32] While PES does not have acidic functional groups, its negative zeta potential is due to adsorption of hydroxyl ions.[44]

Surface roughness influences fouling, with rougher substrates exhibiting greater biofouling and colloidal fouling propensity.[45–48] We determined the RMS roughness (R_{RMS}) of the hydrated substrates using AFM. Representative 2 × 2 μm^2 AFM scans along with average R_{RMS} values are shown in Fig. 7. We observed a relatively smooth interface in the PES substrate with low surface roughness (R_{RMS} = 2.51 ± 0.49 nm, *cf.* Fig. 7 (a)). On the other hand, the grafted PAA chains increase the R_{RMS} of the PES–PAA substrate (R_{RMS} = 5.74 ± 2.18 nm, *cf.* Fig. 7 (b)) compared to the PES control ($p < 0.01$). The negatively charged tethered PAA chains exist in a collapsed (*i.e.*, non-extended) conformation given that the high ionic strength of PBS (162 mM) results in screening of electrostatic repulsions.[49] PAA chain collapse yields the rough, peak-and-valley interfacial structure shown in Fig. 7 (b). Upon edge-tethering GO nanosheets to the PAA surface, we observe an interface with lower R_{RMS} (R_{RMS} = 3.63 ± 1.17 nm, *cf.* Fig. 7 (c)) compared to PES–PAA ($p = 0.03$). GO nanosheets appear to cover the rougher PAA interfacial features, thus decreasing R_{RMS}. This "smoothing over" is possibly caused by GO nanosheets tethered to the PAA layer

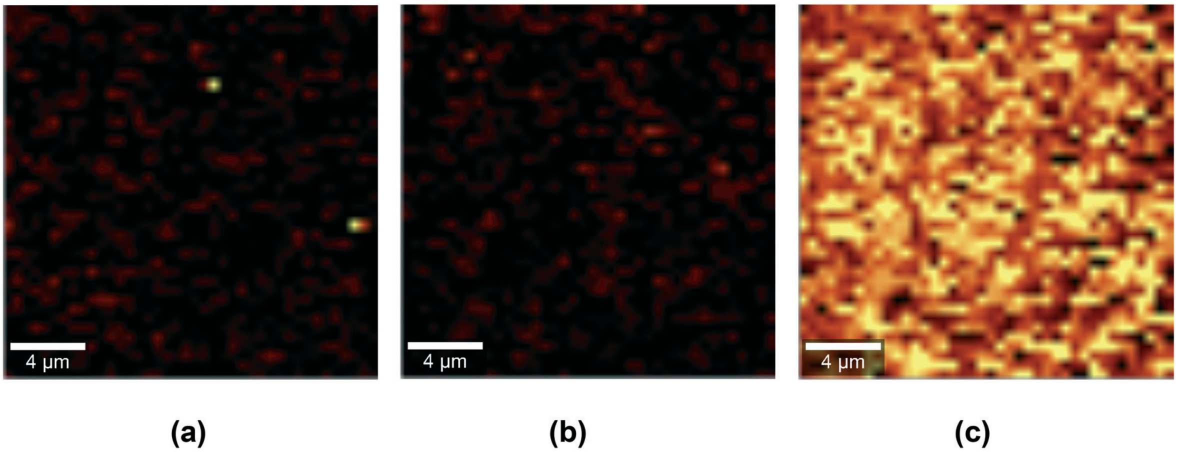

Fig. 5 Raman spectroscopy maps of (a) pristine PES, (b) poly(acrylic acid) (PAA)-modified PES (PES–PAA), and (c) GO-modified PES (PES–GO) substrates.

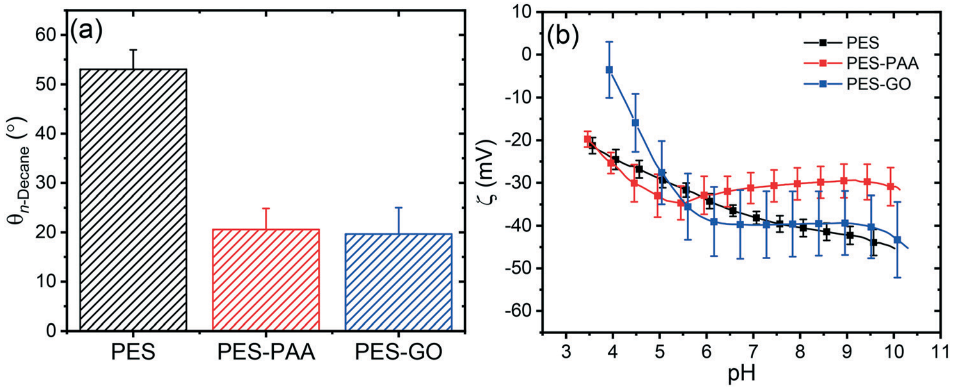

Fig. 6 (a) Contact angles of *n*-decane droplets ($\theta_{n\text{-Decane}}$) on the various substrates, determined in ultrapure water *via* the captive bubble technique. Error bars denote one standard deviation ($n \geq 14$). (b) ζ-Potential as a function of pH of pristine PES, poly(acrylic acid) (PAA)-modified PES (PES–PAA), and GO-modified PES (PES–GO) substrates. The ζ-potential results shown for each substrate type are the average of three independently modified specimens (error bars indicate one standard deviation).

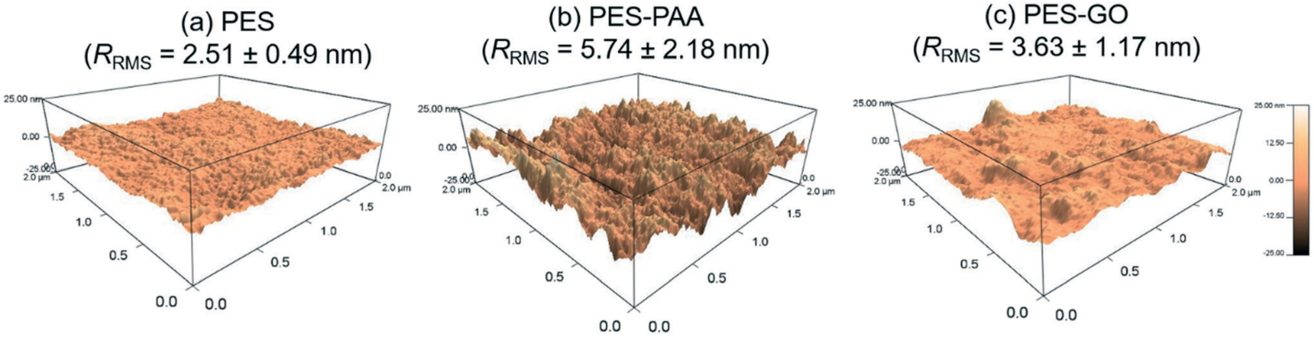

Fig. 7 AC mode AFM images of (a) pristine PES, (b) poly(acrylic acid) (PAA)-modified PES (PES–PAA), and (c) GO-modified PES (PES–GO) substrates. The caption denotes the root-mean-squared roughness (R_{RMS}) computed from eight 1 × 1 μm^2 sections sampled over two different 5 × 5 μm^2 scans of each substrate type. AFM scans and R_{RMS} were obtained in PBS (pH 7.4).

through multiple sites along the sheet periphery (effectively acting as a crosslinker of PAA chains).

Bacterial adhesion. We now investigate bacterial adhesion onto GO-functionalized substrates. Our aim is to examine whether GO substrate functionalization mitigates bacterial adhesion, the first step in biofouling. GO coatings that are both biocidal and anti-adhesive are preferable to those that afford only bacterial inactivation (without preventing bacteria, and bacterial debris, from adsorbing). While previous work on GO-functionalized polyamide membranes has shown that GO coatings may exert dual biocidal/anti-adhesive functions,[20] recent studies have shown that GO nanosheets increase the adhesiveness of inert Si substrates[22] and weakly adhesive polymeric spacer substrates.[23] Here we explain these seemingly contradictory results. Lastly, we elucidate the molecular determinants of adhesion by analyzing the interactions of bacterial adhesin molecules (proteinaceous structures such as pili and outer membrane proteins[50,51]) with the various substrates.

A representative force–distance curve, showing a typical extension–retraction force cycle, is presented in Fig. 8. For each retraction force curve, we recorded the peak adhesion force, F_{Peak}, defined as the binding force with the highest magnitude, and the rupture separation, R, *i.e.*, the separation at which cell–substrate forces vanish (*cf.* Fig. 8). We set the trigger force (F_{Tr}, defined as the force exerted on the bacterium when it contacts the substrate, *cf.* Fig. 8), to 600 pN; this value is of the same order of magnitude as the permeation drag force experienced by similarly-sized colloidal particles during low-pressure membrane filtration.[52]

Fig. 9 (a–c) presents the distribution of *P. fluorescens* peak adhesion forces (F_{Peak}) observed over the different substrates. The "NO" column in the histograms corresponds to measurements in which weak adhesion (< 30 pN, equivalent in magnitude to the noise level in the force) or no adhesion peaks were observed (see Fig. 8 (inset) for a representative non-adhesive force curve).

We observe a broad distribution of peak adhesion forces for all substrates (*cf.* Fig. 9 (a)–(c)), with the majority of adhesion events occurring in the ≈ 0 to 0.5 nN range, typical of bacterial adhesion.[51] Further, we observe that adhesion forces are substrate-dependent. Among the surfaces studied, PES–GO exhibits the lowest probability of adhesion, with 45.9% of measurements showing no-adhesion events, compared to 22.2% for PES–PAA and 32.3% for PES. We observe three consecutive non-adhesive force curves in 15% (PES–PAA), 21% (PES), and 25% (PES–GO) of the loci probed, *i.e.*, a similar trend to that of the probability of observing non-adhesive events across the whole surface. Consistent with the (quasi-static) AFM measurements, bacterial deposition experiments (Fig. S2†) show that the extent of irreversible adhesion is lowest on PES–GO. Fig. 9 (d), presenting the average of all forces ($\bar{F}_{\text{Peak}}$), shows that adhesion is strongest on PES, while PES–GO displays the weakest mean adhesion: $\bar{F}_{\text{Peak}} = -0.11$ (± 0.17) nN for PES–GO *vs.* −0.18 (± 0.18) nN for PES ($p = 0.006$). PES–PAA substrates also demonstrated weaker adhesions ($\bar{F}_{\text{Peak}} = -0.13$ (± 0.11) nN) compared to PES ($p = 0.008$), while similar adhesiveness was displayed by PES–PAA and PES–GO ($p = 0.6$).

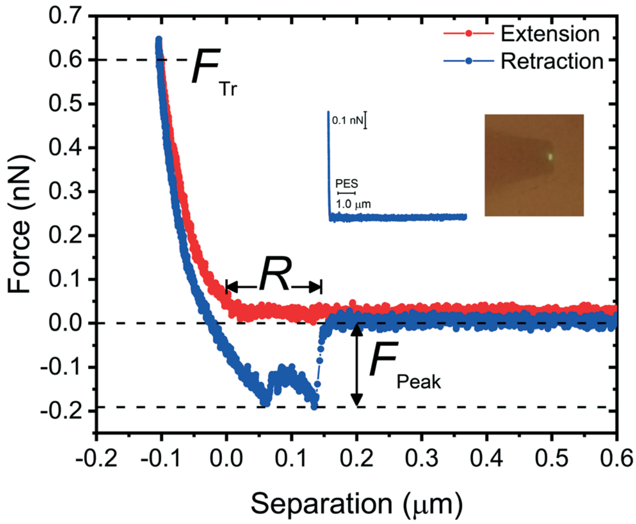

Fig. 8 Representative extension–retraction force cycle recorded over PES with a *P. fluorescens* bacterial probe. The curve shows the definition of the trigger force (F_{Tr}), peak adhesion force (F_{Peak}), and rupture separation (R). The inset shows a representative non-adhesive retraction force curve recorded over PES, and a digital image of a bacterial probe.

A more nuanced adhesion behavior arises when we exclude the non-adhesive measurements from the calculation of the mean. The results, presented in Fig. 9 (e), show that PES substrates still reveal the strongest mean adhesion, *i.e.*, $\bar{F}_{\text{Peak}} = -0.27$ (± 0.15) nN. On the other hand, PES–PAA exhibits the weakest mean adhesion forces with $\bar{F}_{\text{Peak}} = -0.16$ (± 0.10) nN, compared to −0.21 (± 0.18) nN for PES–GO ($p = 0.04$). Consequently, Fig. 9 shows that, while PES–GO surfaces display the lowest probability of *P. fluorescens* attachment (*i.e.*, highest incidence of non-adhesion events, as shown in Fig. 9 (c)), adhering bacteria engage the GO substrate with forces that are stronger than those observed over PES–PAA, and only somewhat weaker than those observed over PES (Fig. 9 (e)).

The picture emerging from Fig. 9 indicates that edge-tethering GO to a PAA coating decreases the mean adhesion force ($\bar{F}_{\text{Peak}}$) of *P. fluorescens* compared to the unmodified PES surface (*cf.* Fig. 9 (d)). However, it is important to note that the lower $\bar{F}_{\text{Peak}}$ observed on PES–GO (Fig. 9 (d)) is due to a high incidence of non-adhesive events on the GO-functionalized substrate (*cf.* Fig. 9 (c)), which offsets the relatively strong adhesion forces exhibited by cells that do successfully adhere to the PES–GO surface (Fig. 9 (e)).

Fig. 10 presents the distribution of the rupture separation (R) over the different substrates. R is also distributed broadly, with mean values ($\bar{R}$) around 1 μm that are a reflection of the adhesins, namely pili and flagella, that mediate *P. fluorescens* binding to substrates.[53–55] Fig. 10 further shows that longer ranged interactions are observed over PES ($\bar{R} = 1.2$ (± 0.9 μm)) compared to PES–PAA ($\bar{R} = 0.7$ (± 1.0 μm), $p = 0.002$) and to PES–GO ($\bar{R} = 0.8$ (± 0.5 μm), $p = 0.008$), suggesting that more sites along individual adhesins bind to the PES substrate. It is also possible that higher $\bar{R}$ observed on the PES substrate indicates that several adhesins of different contour length mediate attachment on PES.[36] R thus displays behavior in line with the adhesion forces reported in Fig. 9 (d), since longer ranged forces are observed on more adhesion-prone PES substrates. Moreover, in view of the lower $\bar{R}$ observed over PES–GO and PES–PAA, Fig. 10 shows that the

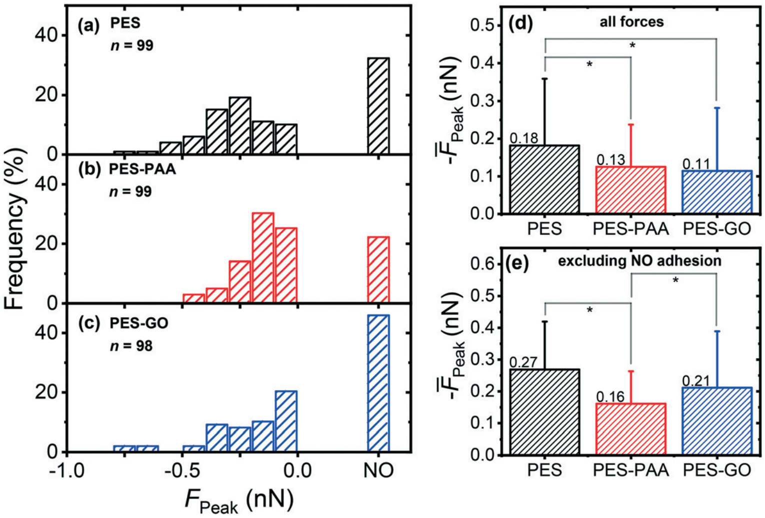

Fig. 9 Distribution of peak adhesion forces (F_{Peak}) of single *P. fluorescens* cells on: (a) pristine PES; (b) poly(acrylic acid) (PAA)-modified PES (PES–PAA); (c) GO-modified PES (PES–GO). The inset shows the number of force measurements (*n*). Measurements were performed in PBS at pH 7.4. (d) Mean peak adhesion forces ($\bar{F}_{Peak}$) computed from (a)–(c), including non-adhesive events (F_{Peak} = 0 nN). (e) Mean peak adhesion forces excluding non-adhesive events. Error bars in (d) and (e) indicate the standard deviation. Pairwise comparisons denoted by * indicate statistical significance ($p < 0.05$).

range of cell adhesion forces is determined by microbial adhesins, and that extension of poly(acrylic acid) chains during cell pull-off does not contribute significantly to *R*.

We turn to the interfacial properties presented in Fig. 6 and 7 to explain the differences in adhesive behavior among the three substrate types. Weakening of cell–substrate forces in PES–PAA (*cf.* Fig. 9 (d and e)) compared to PES is due to the PAA coatings resulting in more hydrophilic substrates (*cf.* Fig. 6 (a)), which mitigate adhesion of *P. fluorescens* bacteria reliant on hydrophobic interactions.[36,53,56] In addition, PAA chain compression results in a steric repulsive force that contributes to weaker bioadhesion.[57,58] We note that long-range electrostatic repulsive forces, involving the negatively charged substrate (Fig. 6 (b)) and bacterium, are absent in PBS (Debye length = 0.75 nm). We observe two effects upon functionalization with GO. First, an increase in the frequency of non-adhesive events compared to PES and PES–PAA (*cf.* "NO" column in Fig. 9 (a–c)), which we attribute to the layer of GO nanosheets that is covalently tethered to PES–PAA; this GO coating lowers the roughness of the interface (*cf.* Fig. 7) thus decreasing adsorption surface area, and results in an additional steric barrier that limits binding of the microbe[22] (similarly, higher surface roughness in PES–PAA explains its lower incidence of non-adhesive events compared to PES). Second, we observe an increase in the mean adhesion force relative to PES–PAA (as shown in Fig. 9 (e), which excludes non-adhesive observations). In view of the similar contact angles of PES–PAA and PES–GO (*cf.* Fig. 6 (a)), the stronger adhesion on the GO-coated substrate cannot be explained by a macroscopic view of hydrophobicity. At the nanoscale, however, GO is known to be amphiphilic, possessing hydrophilic sheet edges,[10] and basal surfaces featuring hydrophobic graphenic domains.[10,59] These nanoscale hydrophobic regions embedded in GO serve as sorption sites for hydrophobic molecules,[60–62] and thus can bolster microbial adhesion through interactions with hydrophobic adhesins.[54]

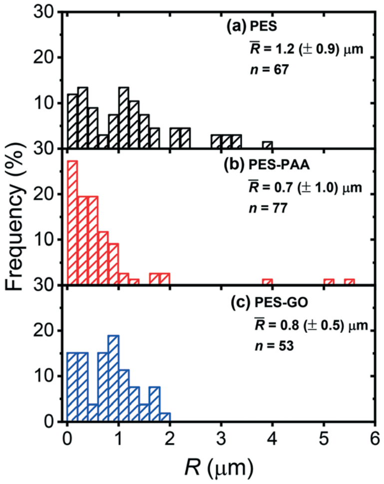

Fig. 10 Distribution of rupture separations (*R*), defined as the distance at which cell adhesion forces vanish, for various substrates: (a) pristine PES; (b) poly(acrylic acid) (PAA)-modified PES (PES–PAA); (c) GO-modified PES (PES–GO). The inset shows the histogram average ($\bar{R}$ (± standard deviation)), and number of measurements (*n*). Measurements were performed in PBS at pH 7.4.

Role of adhesin molecules in microbial adhesion. Fig. 11 and 12 discuss the molecular-level determinants of bacterial adhesion. Force measurements on all three substrates exhibit adhesion peaks such as those shown in Fig. 11, whose characteristic shape results from stretching and unfolding of single biopolymer molecules.[63] Examination of these extension events can therefore provide additional insight into the role of adhesin molecules, such as pili, outer membrane proteins and lipopolysaccharides, in microbial adhesion.[36] Two models are commonly used to describe the elasticity of single biopolymers under force: the worm-like chain (WLC) model, which describes the mechanics of protein domains; and the extended freely-jointed chain (FJC) model, known to describe the elasticity of polysaccharide molecules.[64] In our data only a small fraction of extension events (< 3%) were well described by the FJC model (see Fig. S3† for representative FJC fits on the three substrates); these rare events are due to the extension of polysaccharides on the surface of the bacterial cell, or stretching of PAA chains (known to exhibit FJC mechanics[65]) on the PES–PAA or PES–GO substrate. On the other hand, WLC extension events are far more common, and we analyze them in detail below. We find that 33% of all force measurements collected on PES and PES–PAA substrates, and 26% of measurements collected over PES–GO, exhibit single-molecule extensions that can be quantitatively described by the WLC model. In the WLC model, the elasticity of macromolecules under tension is given by the following force (F)-elongation (z) equation:

$$F(z)=\frac{k_{\mathrm{B}}T}{4L_{\mathrm{p}}}\left[\left(1-\frac{z}{L_{\mathrm{c}}}\right)^{-2}+\frac{4z}{L_{\mathrm{c}}}-1\right] \qquad (1)$$

where L_{p} is the persistence length (a measure of the flexibility of the polymer chain), L_{c} is the contour length (*i.e.*, the total length of the unraveled polymer chain), k_{B} is Boltzmann's constant, and T = 298.15 K is the absolute temperature. Non-linear regression of the force–distance data using the WLC model (carried out with the WLC fitting function in IGOR Pro 6.3) results in best-fit L_{p} estimates (Fig. 12 (a)) across all substrates with an average value $\bar{L}_{\mathrm{p}} \approx 0.3$ nm, in line with the persistence length of proteins,[63,66,67] thus suggesting outer membrane proteins (such as LapA in *P. fluorescens*[51]) as the adhesins mediating microbial attachment.

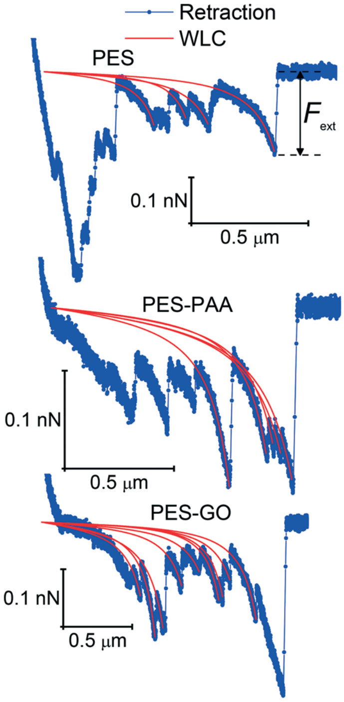

Fig. 11 Enlarged view of retraction force curves, showing single-molecule extension events and corresponding worm-like chain (WLC) fits for various substrates, indicated in the caption.

We further observe multiple WLC events in a single force measurement (*cf.* Fig. 11), allowing us to calculate the number of WLC extensions per force curve (N_{WLC}), as shown in Fig. 12 (b). While WLC events are observed in fewer PES–GO force curves (26% compared to 33% for the other substrates), the mean values ($\bar{N}_{\mathrm{WLC}}$) are similar for PES–GO and PES, *i.e.*, 2.3 ± 2.1 and 2.7 ± 2.2, respectively (p = 0.5). Further PES–PAA exhibits lower $\bar{N}_{\mathrm{WLC}}$ (1.4 ± 0.9) compared to PES and PES–GO ($p < 0.05$). Considering that N_{WLC} is proportional to the number of adhesins that attach to the substrate, the values of $\bar{N}_{\mathrm{WLC}}$ are consistent with the adhesion properties described previously in Fig. 9 (e), which showed that (provided non-adhesive events are excluded) PES and PES–GO showed similar mean adhesion forces.

The single-molecule extension events presented in Fig. 11 (along with corresponding WLC fits) show the occurrence of consecutive single-molecule extensions. This allows determination of the length scale of the extended biomolecule domains from $\Delta L_{\mathrm{c}} = L_{\mathrm{c},i+1} - L_{\mathrm{c},i}$, where $L_{\mathrm{c},i}$ and $L_{\mathrm{c},i+1}$ denote the contour length of two consecutive WLC fits. As shown in Fig. 12 (c), ΔL_{c} is narrowly distributed around mean values $\left(\overline{\Delta L_{\mathrm{c}}}\right)$ of 0.10 (± 0.06) µm and 0.11 (± 0.10) µm for PES–PAA and PES–GO, respectively, whereas for PES we observe a much broader distribution with $\overline{\Delta L_{\mathrm{c}}}$ = 0.24 (± 0.18) µm. The tight distribution of ΔL_{c} around ~100 nm suggests that the WLC events observed on PES–GO and PES–PAA are likely due to proteinaceous adhesins whose domains unravel sequentially in pairs or triplets (the contour length of cell membrane and pilin proteins is 30–60 nm[51,68]), as was recently proposed for *P. fluorescens* adhesins.[51] On the other hand, the much broader distribution observed over PES substrates could be the result of two distinct phenomena. Firstly, desorption of two different adhesin molecules of disparate lengths,[53] resulting in two sequential WLC peaks characterized by a large ΔL_{c}; the longer rupture separation observed on PES compared to the other two surfaces (see Fig. 10) supports this mechanism. Alternatively, the more hydrophobic character of PES substrates (Fig. 6 (a)) could lead to surface-induced partial unfolding of adhesin molecules,[36] the corresponding change in protein conformation leading to a wider range of ΔL_{c} values. Finally, Fig. 12 (d) presents the distribution of extension forces (F_{ext}), defined as the force at each peak observed in a single-molecule extension event (*cf.* Fig. 11, top panel). The magnitude of the forces is in the range of 100–300 pN, in agreement with previous reports for unfolding forces of protein domains,[51,63] with the average value ($\bar{F}_{\mathrm{ext}}$) being similar for all substrates. This suggests that F_{ext} is primarily due to the elastic response of adhesins to the

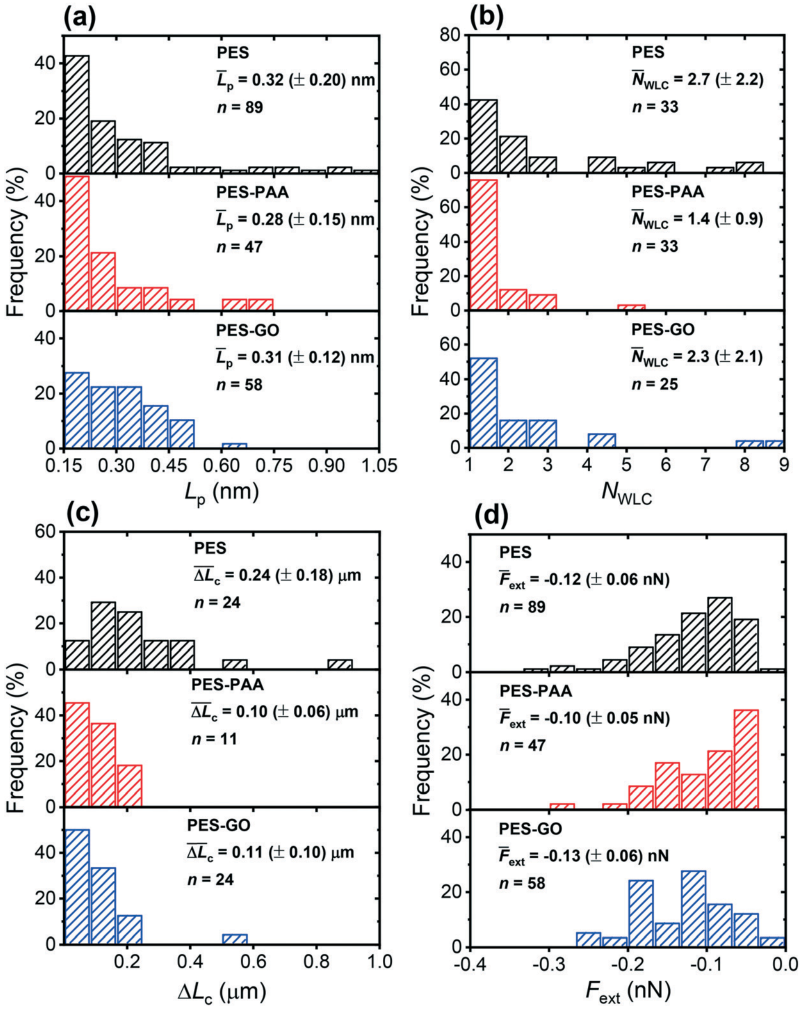

Fig. 12 (a) Distribution of best-fit persistence length values (L_p), obtained from WLC model fits on various substrates (see Fig. 11 for representative fits). (b) Distribution of the number of WLC single-molecule extension events per force curve (N_{WLC}). (c) Distribution of ΔL_c (the difference in contour length (L_c) between two consecutive WLC extension events). (d) Distribution of extension forces (F_{ext}, the force measured at the each WLC extension peak). The caption of each figure indicates the substrate type, histogram average ($\bar{L}_p$, $\bar{N}_{WLC}$, $\overline{\Delta L}_c$, $\bar{F}_{ext}$ (± standard deviation)) and number of measurements (*n*).

external force, and that desorption from the substrate does not contribute significantly to the extension force.[63]

4. Conclusions

While graphene oxide (GO) has shown strong biocidal activity,[12,13,19,69] there have been conflicting reports as to whether GO can mitigate bacterial adhesion,[22,23] the first step of biofilm formation and biofouling. This paper used single-cell force spectroscopy to show that edge-tethering GO nanosheets to poly(acrylic acid) (PAA) brushes produces GO coatings (formed on polyethersulfone (PES) substrates) characterized by low *P. fluorescens* adhesion forces. Our results show that lower mean adhesion forces observed on GO-functionalized coatings (designated PES–GO) are mainly due to the occurrence of cell–substrate repulsive (non-adhesive) forces; these are in turn derived from the hydrophilicity and steric repulsion afforded by the GO-functionalized PAA layer. A salient observation is that GO is not intrinsically anti-adhesive: its integration into a polymeric brush is essential to achieve a low-adhesion interface. GO-free PAA coatings (termed PES–PAA) also demonstrated lower bacterial adhesion due to their hydrophilicity. In the absence of PAA or GO, PES control substrates exhibited stronger bacterial adhesion due to their hydrophobicity. Analysis of the force spectroscopy data on all substrates shows that adhesion of *P. fluorescens* is driven by proteinaceous adhesins, whose elasticity is well described by the worm-like chain model.

Our results highlight the importance of interfacial properties (*e.g.*, surface roughness, hydrophilicity) in the formulation of GO-based antibacterial interfaces for environmental applications, pointing out possible directions for future study. In the context of water treatment systems, it is necessary to characterize bioadhesion to GO interfaces (such as those in membranes,[19,20] spacers,[23] and adsorbents[7]), under realistic hydrodynamic conditions.

Conflicts of interest

There are no conflicts of interest to declare.

Acknowledgements

This work was supported by the Environment and Natural Resources Trust Fund, as recommended by the Legislative-Citizen Commission on Minnesota Resources. Portions of this work were carried out in the Characterization Facility at UMN, supported by NSF through award DMR-1420013, and at the Minnesota Nano Center, which receives partial support from NSF through the National NanoCoordinated Infrastructure Network (NNCI) (Award Number ECCS-1542202). SRVC is grateful to 3M Co. for a Non-Tenured Faculty Award.

References

1 K. S. Novoselov, A. K. Geim, S. V. Morozov, D. Jiang, Y. Zhang and S. V. Dubonos, *et al.* Electric field in atomically thin carbon films, *Science*, 2004, **306**(5696), 666–669.

2 P. J. J. Alvarez, C. K. Chan, M. Elimelech, N. J. Halas and D. Villagrán, Emerging opportunities for nanotechnology to enhance water security, *Nat. Nanotechnol.*, 2018, **13**(8), 634–641.

3 Y. Zhu, S. Murali, W. Cai, X. Li, J. W. Suk and J. R. Potts, *et al.* Graphene and graphene oxide: Synthesis, properties, and applications, *Adv. Mater.*, 2010, **22**(35), 3906–3924.

4 R. K. Joshi, P. Carbone, F. C. Wang, V. G. Kravets, Y. Su and I. V. Grigorieva, *et al.* Precise and ultrafast molecular sieving through graphene oxide membranes, *Science*, 2014, **343**(6172), 752–754.

5 S. C. O'Hern, M. S. H. Boutilier, J. C. Idrobo, Y. Song, J. Kong and T. Laoui, *et al.* Selective ionic transport through tunable subnanometer pores in single-layer graphene membranes, *Nano Lett.*, 2014, **14**(3), 1234–1241.

6 M. Hu and B. Mi, Enabling graphene oxide nanosheets as water separation membranes, *Environ. Sci. Technol.*, 2013, **47**(8), 3715–3723.

7 N. Yousefi, X. Lu, M. Elimelech and N. Tufenkji, Environmental performance of graphene-based 3D macrostructures, *Nat. Nanotechnol.*, 2019, **14**(2), 107–119, DOI: 10.1038/s41565-018-0325-6.

8 Y. Yang, R. Zhao, T. Zhang, K. Zhao, P. Xiao and Y. Ma, *et al.* Graphene-Based Standalone Solar Energy Converter for Water Desalination and Purification, *ACS Nano*, 2018, **12**(1), 829–835, DOI: 10.1021/acsnano.7b08196.

9 F. Perreault, A. Fonseca De Faria and M. Elimelech, Environmental applications of graphene-based nanomaterials, *Chem. Soc. Rev.*, 2015, **44**(16), 5861–5896.

10 V. C. Sanchez, A. Jachak, R. H. Hurt and A. B. Kane, Biological interactions of graphene-family nanomaterials: An interdisciplinary review, *Chem. Res. Toxicol.*, 2012, **25**(1), 15–34.

11 J. Chen, H. Peng, X. Wang, F. Shao, Z. Yuan and H. Han, Graphene oxide exhibits broad-spectrum antimicrobial activity against bacterial phytopathogens and fungal conidia by intertwining and membrane perturbation, *Nanoscale*, 2014, **6**(3), 1879–1889, Available from: http://xlink.rsc.org/?DOI=C3NR04941H.

12 W. Hu, C. Peng, W. Luo, M. Lv, X. Li and D. Li, *et al.* Graphene-based antibacterial paper, *ACS Nano*, 2010, **4**(7), 4317–4323.

13 F. Perreault, A. F. De Faria, S. Nejati and M. Elimelech, Antimicrobial Properties of Graphene Oxide Nanosheets: Why Size Matters, *ACS Nano*, 2015, **9**(7), 7226–7236.

14 S. Gurunathan, J. W. Han, A. A. Dayem, V. Eppakayala and J. H. Kim, Oxidative stress-mediated antibacterial activity of graphene oxide and reduced graphene oxide in Pseudomonas aeruginosa, *Int. J. Nanomed.*, 2012, **7**, 5901–5914.

15 H. R. Chae, J. Lee, C. H. Lee, I. C. Kim and P. K. Park, Graphene oxide-embedded thin-film composite reverse osmosis membrane with high flux, anti-biofouling, and chlorine resistance, *J. Membr. Sci.*, 2015, **483**, 128–135.

16 M. E. A. Ali, L. Wang, X. Wang and X. Feng, Thin film composite membranes embedded with graphene oxide for water desalination, *Desalination*, 2016, **386**, 67–76.

17 A. Inurria, P. Cay-Durgun, D. Rice, H. Zhang, D. K. Seo and M. L. Lind, *et al.* Polyamide thin-film nanocomposite membranes with graphene oxide nanosheets: Balancing membrane performance and fouling propensity, *Desalination*, 2018, **451**, 139–147.

18 X. Lu, X. Feng, X. Zhang, M. N. Chukwu, C. O. Osuji and M. Elimelech, Fabrication of a Desalination Membrane with Enhanced Microbial Resistance through Vertical Alignment of Graphene Oxide, *Environ. Sci. Technol. Lett.*, 2018, **5**(10), 614–620.

19 F. Perreault, M. E. Tousley and M. Elimelech, Thin-Film Composite Polyamide Membranes Functionalized with Biocidal Graphene Oxide Nanosheets, *Environ. Sci. Technol. Lett.*, 2013, **1**(1), 71–76.

20 F. Perreault, H. Jaramillo, M. Xie, M. Ude, L. D. Nghiem and M. Elimelech, Biofouling Mitigation in Forward Osmosis Using Graphene Oxide Functionalized Thin-Film Composite Membranes, *Environ. Sci. Technol.*, 2016, **50**(11), 5840–5848.

21 Y. F. Dufrene, Sticky microbes: Forces in microbial cell adhesion, *Trends Microbiol.*, 2015, **23**(6), 376–382.

22 J. Xue, S. BinAhmed, Z. Wang, N. G. Karp, B. L. Stottrup and S. Romero-Vargas Castrillón, Bacterial Adhesion to Graphene Oxide (GO)-Functionalized Interfaces Is Determined by Hydrophobicity and GO Sheet Spatial Orientation, *Environ. Sci. Technol. Lett.*, 2018, **5**(1), 14–19.

23 D. Rice, A. C. Barrios, Z. Xiao, A. Bogler, E. Bar-Zeev and F. Perreault, Development of anti-biofouling feed spacers to improve performance of reverse osmosis modules, *Water Res.*, 2018, **145**, 599–607.

24 S. Kang and M. Elimelech, Bioinspired single bacterial cell force spectroscopy, *Langmuir*, 2009, **25**(17), 9656–9659.

25 S. M. Hinsa, M. Espinosa-Urgel, J. L. Ramos and G. A. O'Toole, Transition from reversible to irreversible attachment during biofilm formation by Pseudomonas fluorescens WCS365 requires an ABC transporter and a large secreted protein, *Mol. Microbiol.*, 2003, **49**(4), 905–918.

26 I. E. Ivanov, C. D. Boyd, P. D. Newell, M. E. Schwartz, L. Turnbull and M. S. Johnson, *et al.* Atomic force and super-resolution microscopy support a role for LapA as a cell-surface biofilm adhesin of Pseudomonas fluorescens, *Res. Microbiol.*, 2012, **163**(9–10), 685–691.

27 H. Wang and H. R. Brown, Self-initiated photopolymerization and photografting of acrylic monomers, *Macromol. Rapid Commun.*, 2004, **25**(11), 1095–1099.

28 J. Deng, L. Wang, L. Liu and W. Yang, Developments and new applications of UV-induced surface graft polymerizations, *Prog. Polym. Sci.*, 2009, **34**(2), 156–193.

29 B. Van Der Bruggen, Chemical modification of polyethersulfone nanofiltration membranes: A review, *J. Appl. Polym. Sci.*, 2009, **114**(1), 630–642.

30 E. Igbinigun, Y. Fennell, R. Malaisamy, K. L. Jones and V. Morris, Graphene oxide functionalized polyethersulfone membrane to reduce organic fouling, *J. Membr. Sci.*, 2016, **514**, 518–526.

31 M. Homayoonfal, A. Akbari and M. R. Mehrnia, Preparation of polysulfone nanofiltration membranes by UV-assisted grafting polymerization for water softening, *Desalination*, 2010, **263**(1–3), 217–225.

32 D. Li, M. B. Müller, S. Gilje, R. B. Kaner and G. G. Wallace, Processable aqueous dispersions of graphene nanosheets, *Nat. Nanotechnol.*, 2008, 3(2), 101–105, Available from: http://www.nature.com/doifinder/10.1038/nnano.2007.451.

33 K. N. Kudin, B. Ozbas, H. C. Schniepp, R. K. Prud'homme, I. A. Aksay and R. Car, Raman spectra of graphite oxide and functionalized graphene sheets, *Nano Lett.*, 2008, **8**(1), 36–41.

34 Z. Grabarek and J. Gergely, Zero-length crosslinking procedure with the use of active esters, *Anal. Biochem.*, 1990, **185**(1), 131–135.

35 S. L. Walker, S. Bhattacharjee, E. M. V. Hoek and M. Elimelech, A novel asymmetric clamping cell for measuring streaming potential of flat surfaces, *Langmuir*, 2002, **18**(6), 2193–2198.

36 S. Binahmed, A. Hasane, Z. Wang, A. Mansurov and S. Romero-Vargas Castrillón, Bacterial Adhesion to Ultrafiltration Membranes: Role of Hydrophilicity, Natural Organic Matter, and Cell-Surface Macromolecules, *Environ. Sci. Technol.*, 2018, **52**(1), 162–172.

37 H. Ma, R. H. Davis and C. N. Bowman, Novel sequential photoinduced living graft polymerization, *Macromolecules*, 2000, **33**(2), 331–335.

38 C. Klaysom, B. P. Ladewig, G. Q. M. Lu and L. Wang, Preparation and characterization of sulfonated polyethersulfone for cation-exchange membranes, *J. Membr. Sci.*, 2011, **368**(1–2), 48–53.

39 E. Pretsch, P. Bühlmann and C. Affolter, *Structure Determination of Organic Compounds*, Springer, 3rd edn, 2000, p. 338.

40 L. Wang, X. Song, T. Wang, S. Wang, Z. Wang and C. Gao, Fabrication and characterization of polyethersulfone/carbon nanotubes (PES/CNTs) based mixed matrix membranes (MMMs) for nanofiltration application, *Appl. Surf. Sci.*, 2015, **330**, 118–125.

41 P. J. Evans, M. R. Bird, A. Pihlajamäki and M. Nyström, The influence of hydrophobicity, roughness and charge upon ultrafiltration membranes for black tea liquor clarification, *J. Membr. Sci.*, 2008, **313**(1–2), 250–262.

42 A. Weis, M. R. Bird, M. Nyström and C. Wright, The influence of morphology, hydrophobicity and charge upon the long-term performance of ultrafiltration membranes fouled with spent sulphite liquor, *Desalination*, 2005, **175**(1 SPEC. ISS), 73–85.

43 H. Susanto and M. Ulbricht, Characteristics, performance and stability of polyethersulfone ultrafiltration membranes prepared by phase separation method using different macromolecular additives, *J. Membr. Sci.*, 2009, **327**(1–2), 125–135.

44 S. Kasemset, Z. He, D. J. Miller, B. D. Freeman and M. M. Sharma, Effect of polydopamine deposition conditions on polysulfone ultrafiltration membrane properties and threshold flux during oil/water emulsion filtration, *Polymer*, 2016, **97**, 247–257.

45 N. Park, B. Kwon, I. S. Kim and J. Cho, Biofouling potential of various NF membranes with respect to bacteria and their soluble microbial products (SMP): Characterizations, flux decline, and transport parameters, *J. Membr. Sci.*, 2005, **258**(1–2), 43–54.

46 M. Pasmore, P. Todd, S. Smith, D. Baker, J. A. Silverstein and D. Coons, *et al.* Effects of ultrafiltration membrane surface properties on Pseudomonas aeruginosa biofilm initiation for the purpose of reducing biofouling, *J. Membr. Sci.*, 2001, **194**(1), 15–32.

47 E. M. Vrijenhoek, S. Hong and M. Elimelech, Influence of membrane surface properties on initial rate of colloidal fouling of reverse osmosis and nanofiltration membranes, *J. Membr. Sci.*, 2001, **188**(1), 115–128.

48 M. Elimelech, X. Zhu, A. E. Childress and S. Hong, Role of membrane surface morphology in colloidal fouling of cellulose acetate and composite aromatic polyamide reverse osmosis membranes, *J. Membr. Sci.*, 1997, **127**(1), 101–109.

49 T. Wu, P. Gong, I. Szleifer, P. Vlček, V. Šubr and J. Genzer, Behavior of surface-anchored poly(acrylic acid) brushes with grafting density gradients on solid substrates: 1. Experiment, *Macromolecules*, 2007, **40**(24), 8756–8764.

50 T. A. Camesano, Y. Liu and M. Datta, Measuring bacterial adhesion at environmental interfaces with single-cell and single-molecule techniques, *Adv. Water Resour.*, 2007, **30**(6–7), 1470–1491.

51 S. El-Kirat-Chatel, A. Beaussart, C. D. Boyd, G. A. O'Toole and Y. F. Dufrêne, Single-cell and single-molecule analysis deciphers the localization, adhesion, and mechanics of the biofilm adhesin LapA, *ACS Chem. Biol.*, 2014, **9**(2), 485–494.

52 A. Ronen, W. Duan, I. Wheeldon, S. Walker and D. Jassby, Microbial Attachment Inhibition through Low-Voltage Electrochemical Reactions on Electrically Conducting Membranes, *Environ. Sci. Technol.*, 2015, **49**(21), 12741–12750.

53 G. Zeng, T. Müller and R. L. Meyer, Single-cell force spectroscopy of bacteria enabled by naturally derived proteins, *Langmuir*, 2014, **30**(14), 4019–4025.

54 S. J. Vesper, Production of Pili (Fimbriae) by Pseudomonas fluorescens and Correlation with Attachment to Corn Roots, *Appl. Environ. Microbiol.*, 1987, **53**(7), 1397–1405, Available from: http://www.ncbi.nlm.nih.gov/pubmed/16347370%5Cnhttp://www.pubmedcentral.nih.gov/articlerender.fcgi?artid=PMC203883.

55 N. Dasgupta, S. K. Arora and R. Ramphal, *The Flagellar System of Pseudomonas aeruginosa BT - Pseudomonas: Volume 1 Genomics, Life Style and Molecular Architecture*, ed. J.-L. Ramos, Springer US, Boston, MA, 2004, pp. 675–698, DOI: 10.1007/978-1-4419-9086-0_22.

56 Y. L. Ong, A. Razatos, G. Georgiou and M. M. Sharma, Adhesion forces between E. coli bacteria and biomaterial surfaces, *Langmuir*, 1999, **15**(8), 2719–2725.

57 S. Pasche, M. Textor, L. Meagher, N. D. Spencer and H. J. Griesser, Relationship between interfacial forces measured by colloid-probe atomic force microscopy and protein resistance of poly(ethylene glycol)-grafted poly(L-lysine) adlayers on niobia surfaces, *Langmuir*, 2005, **21**(14), 6508–6520.

58 S. Gon, K. N. Kumar, K. Nüsslein and M. M. Santore, How bacteria adhere to brushy PEG surfaces: Clinging to flaws and compressing the brush, *Macromolecules*, 2012, **45**(20), 8373–8381.

59 K. Erickson, R. Erni, Z. Lee, N. Alem, W. Gannett and A. Zettl, Determination of the local chemical structure of graphene oxide and reduced graphene oxide, *Adv. Mater.*, 2010, **22**(40), 4467–4472.

60 L. J. Cote, J. Kim, V. C. Tung, J. Luo, F. Kim and J. Huang, Graphene oxide as surfactant sheets, *Pure Appl. Chem.*, 2010, **83**(1), 95–110, Available from: https://www.degruyter.com/view/j/pac.2011.83.issue-1/pac-con-10-10-25/pac-con-10-10-25.xml.

61 J. Kim, L. J. Cote, F. Kim, W. Yuan, K. R. Shull and J. Huang, Graphene oxide sheets at interfaces, *J. Am. Chem. Soc.*, 2010, **132**(23), 8180–8186.

62 Z. Liu, J. T. Robinson, X. Sun and H. Dai, PEGylated nanographene oxide for delivery of water-insoluble cancer drugs, *J. Am. Chem. Soc.*, 2008, **130**(33), 10876–10877.

63 M. Rief, M. Gautel, F. Oesterhelt, J. M. Fernandez and H. E. Gaub, Reversible Unfolding of Individual Titin Immunoglobulin Domains by AFM, *Science*, 1997, **276**(5315), 1109–1112, DOI: 10.1126/science.276.5315.1109.

64 G. Francius, D. Alsteens, V. Dupres, S. Lebeer, S. De Keersmaecker and J. Vanderleyden, *et al.* Stretching polysaccharides on live cells using single molecule force spectroscopy, *Nat. Protoc.*, 2009, **4**(6), 939–946.

65 H. Li, B. Liu, X. Zhang, C. Gao, J. Shen and G. Zou, Single-molecule force spectroscopy on poly(acrylic acid) by AFM, *Langmuir*, 1999, **15**(6), 2120–2124.

66 G. Stirnemann, D. Giganti, J. M. Fernandez and B. J. Berne, Elasticity, structure, and relaxation of extended proteins under force, *Proc. Natl. Acad. Sci. U. S. A.*, 2013, **110**(10), 3847–3852, DOI: 10.1073/pnas.1300596110.

67 M. Carrion-Vazquez, A. F. Oberhauser, S. B. Fowler, P. E. Marszalek, S. E. Broedel and J. Clarke, *et al.* Mechanical and chemical unfolding of a single protein: a comparison, *Proc. Natl. Acad. Sci. U. S. A.*, 1999, **96**(7), 3694–3699, Available from: http://www.ncbi.nlm.nih.gov/pubmed/10097099%0Ahttp://www.pubmedcentral.nih.gov/articlerender.fcgi?artid=PMC22356.

68 A. Filloux, S. de Bentzmann, M. Aurouze, A. Lazdunski and I. Vallet, Fimbrial Genes in *Pseudomonas Aeruginosa* and Pseudomonas Putida, in *Pseudomonas*, ed. J. L. Ramos, 2004, pp. 721–748.

69 O. Akhavan and E. Ghaderi, Toxicity of graphene and graphene oxide nanowalls against bacteria, *ACS Nano*, 2010, **4**(10), 5731–5736.

Electronic Supplementary Material (ESI) for Environmental Science: Nano.
This journal is © The Royal Society of Chemistry 2019

Do Graphene Oxide Nanostructured Coatings Mitigate Bacterial Adhesion?

Electronic Supplementary Information

Karl Wuolo-Journey[1♠], Sara BinAhmed[1♠], Elise Linna[1], Santiago Romero-Vargas Castrillón[1, 2, 3 *]

Environmental Science: Nano

[1] Department of Civil, Environmental, and Geo- Engineering, University of Minnesota,
500 Pillsbury Dr. SE, Minneapolis, MN 55455, USA
[2] Institute for Infrastructure and Environment, School of Engineering,
The University of Edinburgh, William Rankine Building, Thomas Bayes Road,
Edinburgh EH9 3FG United Kingdom
[3] Institute for Materials and Processes, School of Engineering,
The University of Edinburgh, Sanderson Building, Robert Stevenson Road,
Edinburgh EH9 3FB United Kingdom

*Corresponding author:
Santiago Romero-Vargas Castrillón, Santiago@ed.ac.uk, sromerov@umn.edu
Tel: +44(0)131 651 3567

♠These authors contributed equally to this work

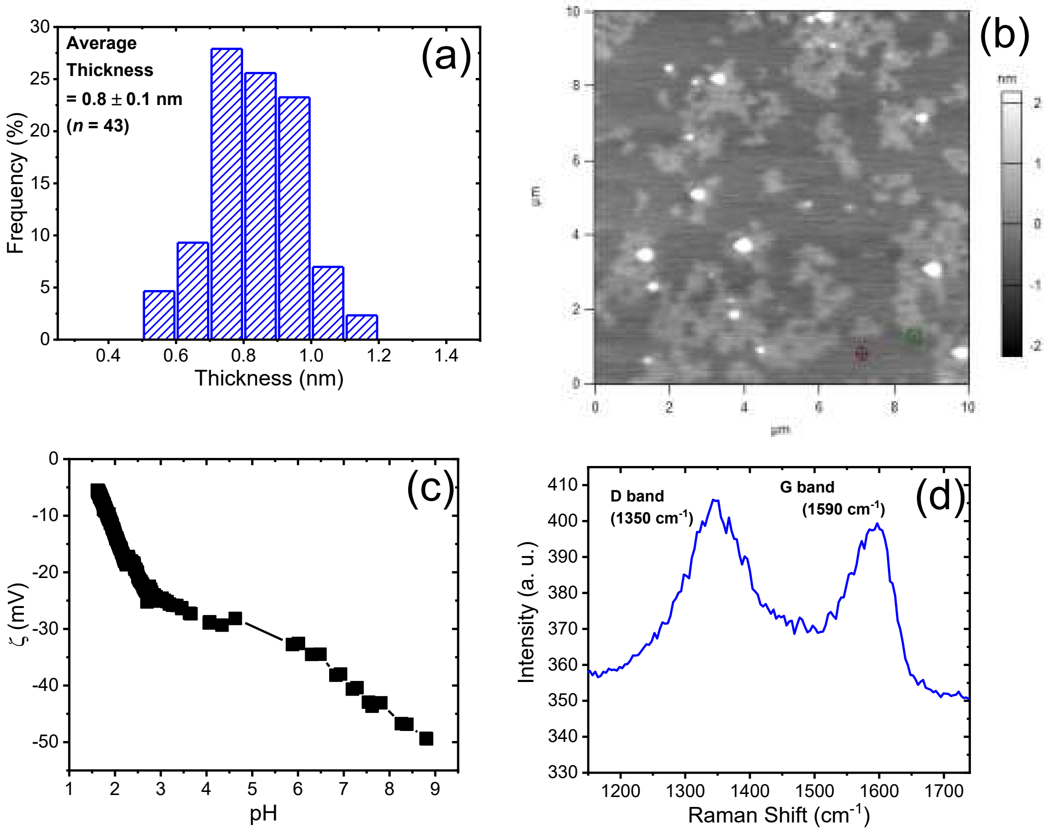

Figure S1. Characterization of graphene oxide (GO) nanosheets: (a) distribution of nanosheet thickness determined by AC mode AFM in air using an AC160TS-R3 Si cantilever (Olympus) with nominal spring constant 26 N m^{-1} and resonance frequency 300 Hz; (b) representative AFM image of GO nanosheets deposited on a Si substrate; (c) ζ-Potential of GO in aqueous dispersion at a concentration of 250 μg mL^{-1}, determined with a Stabino zeta potential analyzer; (d) Raman spectrum of GO nanosheets deposited on a silicon wafer.

Bacterial Deposition Assay. To complement our AFM results, we carried out a bacterial deposition assay to evaluate the bioadhesion propensity of the substrates. The assay entails exposure of the membrane surfaces to a *P. fluorescens* suspension under agitation, followed by colony counting from irreversibly adhered cells.[1] *P. fluorescens* ATCC 13525 was cultured overnight in 50 mL of autoclaved LB broth at 30 °C in an incubator (ThermoScientific MAXQ4450) under stirring (125 rpm). Bacterial suspensions were diluted 1:25 in autoclaved LB broth, and incubated for a further three hours at 175 rpm and 30 °C. Cells were harvested in mid-exponential phase ($OD_{600\ nm} \approx 0.6$) and centrifuged thrice at 5000g (for 1 min), re-suspending the pellet after each centrifugation in 1 mL PBS (pH 7.4). After the final re-suspension, 1-cm^2 substrate coupons were placed at the bottom of scintillation vials and each was immersed in 1 mL of the bacterial suspension, such that the entire coupon was fully covered by the liquid. The scintillation vials were then placed in the incubator (ThermoScientific MAXQ4450) at 30 °C under 175 rpm agitation. After 1 hour, substrates were removed from the suspension, gently rinsed with PBS, and placed in 10 mL of fresh PBS in 50-mL falcon tubes. Following bath sonication for 10 minutes, the resulting suspension was diluted 1:100, and a 50-µL aliquot of the dilution was smeared over an agar plate with a sterilized glass rod. After incubation overnight at 30 °C, the colonies were counted. This experiment was repeated two additional times for each substrate type for a total of three replicates.

The results of the bacterial deposition assay are presented in Fig. S2, showing the number of colony forming units (CFU) normalized by the PES control. Adhesion is significantly mitigated on PES-GO substrates, with the number of colonies on the PES-GO surface being 8.1% of the control PES following a 1-h exposure ($p < 0.05$, one-sided unpaired t-test).

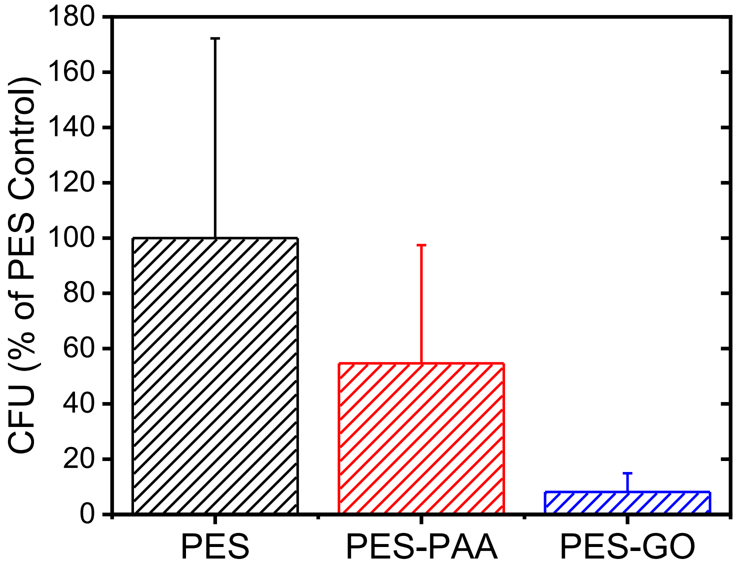

Figure S2. Bacterial deposition assay of pristine PES, poly(acrylic acid) (PAA)-modified PES (PES-PAA), and GO-modified PES (PES-GO) substrates. Colony-forming units (CFU) are shown as % of the PES control. Error bars denote the standard deviation of three experiments.

It is important to note that the CFU data in Fig. S2 are possibly influenced by the cytotoxicity of GO.[1–4] Thus, the precipitous drop in CFU count on PES-GO compared to PES and PES-PAA may be due to a combination of lower adhesion and GO's biocidal activity. However, the relative contributions to the CFU count of adhesion mitigation (due to the interfacial properties of PES-GO) and biocidal activity cannot be disentangled with this simple colony counting assay, and thus would require further investigation.

Characterization of Membrane Transport Properties. The water permeability coefficient (A) of the membranes was determined in a laboratory-scale filtration apparatus equipped with a crossflow cell (CF042D, Sterlitech, with active membrane area, A_m, of 42.1 cm^2), pump (HydraCell M-03S, Wanner Engineering), and temperature-controlled stainless steel feed reservoir. Membranes were compacted with a distilled water feed for 24 hours at a transmembrane pressure difference (Δp) of 50 psi and crossflow velocity of 0.08 m s^{-1}. Following compaction, measurements of the steady-state permeate flow rate were recorded every second for 1 hour at Δp = 50 psi and 20 °C with a digital flow meter (SLI, Sensirion). The average permeate flow rate, Q_p, was used to compute the water permeability coefficient from $A = Q_p/(A_m \Delta p)$. For control polyethersulfone (PES) membranes, the flux through the membranes was determined by weighing the permeate, since the permeate flow rate exceeded the maximum flow rate measurable with the digital flow meter. Four poly(acrylic acid)-modified (PES-PAA), four GO-modified (PES-GO) and two control PES membranes were characterized.

Effect of Surface Functionalization on Water Permeability and Ion Rejection. Surface modification of the PES membranes resulted in additional hydraulic resistance that decreased the water permeability coefficient (A). For pristine PES we find $A = 102.1 \pm 3.5$ L m^{-2} h^{-1} bar^{-1}. On the other hand, for PES-PAA membranes (prepared by acrylic acid polymerization with 10-s UV exposure), we find $A = 9.0 \pm 1.8$ L m^{-2} h^{-1} bar^{-1}, while for PES-GO, $A = 7.0 \pm 0.7$ L m^{-2} h^{-1} bar^{-1}, i.e., the covalently bonded GO layer further decreases water permeability. We also determined the Na_2SO_4 rejection coefficient (R) at $\Delta p = 50$ psi (feed concentration = 10 mM) for the functionalized membranes using a conductivity probe, finding R = 21.4% and 42.7% for PES-GO and PES-PAA, respectively. The A coefficient and ion rejection of PES-PAA and PES-GO materials are similar to those of nanofiltration membranes.[5,6] Additional experiments with PES-PAA membranes prepared with 20-60 sec UV irradiation resulted in steep loss in water permeability (results not shown), due to the formation of a dense PAA layer (observe the prominent carboxyl band at 1700 cm^{-1} when the irradiation time was ≥ 20 s, Fig. 2).

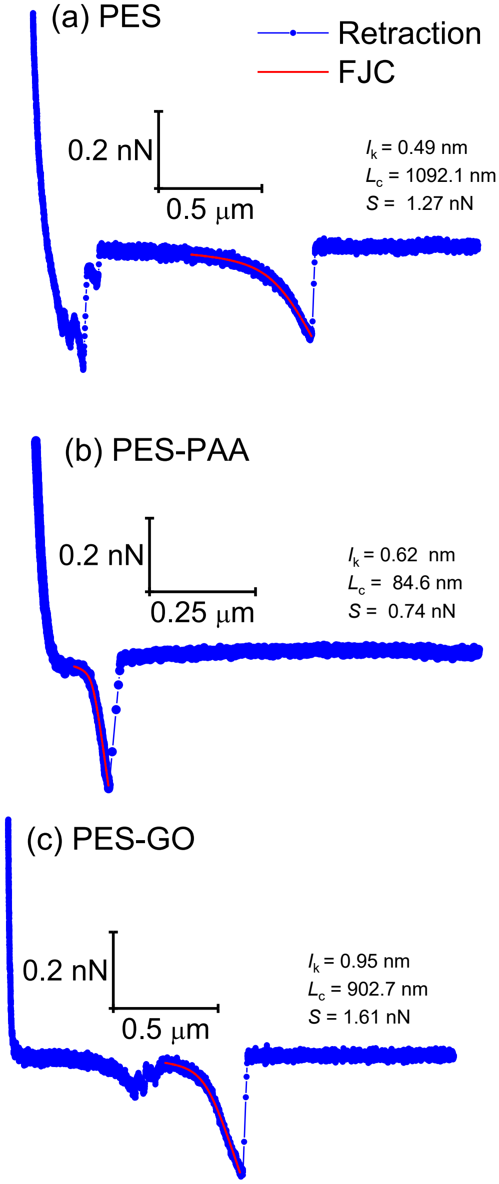

Figure S3. Representative retraction force (F)-elongation (z) curves for different membrane substrates (see caption) recorded with *P. fluorescens* bacterial probes. The data show fits of the extended freely-jointed chain (FJC) model, given by $z(F) = L_{\mathrm{c}}\left[\coth\left(\frac{FI_{\mathrm{k}}}{k_{\mathrm{B}}T}\right) - \frac{k_{\mathrm{B}}T}{FI_{\mathrm{k}}}\right]\left(1 + \frac{F}{S}\right)$, where L_{c} is the contour length, I_{k} is the Kuhn length, and S is the stretch modulus of the polymer; k_{B} and T = 298.15 K are Boltzmann's constant and absolute temperature, respectively. Best-fit values of L_{c}, I_{k} and S are given in the caption. Due to the thermal noise underlying the measurements (≈ 30 pN), the fitted region of the force-extension curves was smoothed using a locally weighted least-squares smoothing algorithm (loess) implemented in Origin 2018 (Northampton, MA). FJC parameters were obtained by non-linear regression of the smoothed data using the function nlinfit in Matlab R2018a (MathWorks, Natick, MA).

Literature Cited

1. Perreault, F., Tousley, M. E. & Elimelech, M. Thin-Film Composite Polyamide Membranes Functionalized with Biocidal Graphene Oxide Nanosheets. *Environ. Sci. Technol. Lett.* **1**, 71–76 (2013).
2. Perreault, F., De Faria, A. F., Nejati, S. & Elimelech, M. Antimicrobial Properties of Graphene Oxide Nanosheets: Why Size Matters. *ACS Nano* **9**, 7226–7236 (2015).
3. Akhavan, O. & Ghaderi, E. Toxicity of graphene and graphene oxide nanowalls against bacteria. *ACS Nano* **4**, 5731–5736 (2010).
4. Gurunathan, S., Han, J. W., Dayem, A. A., Eppakayala, V. & Kim, J. H. Oxidative stress-mediated antibacterial activity of graphene oxide and reduced graphene oxide in Pseudomonas aeruginosa. *Int. J. Nanomedicine* **7**, 5901–5914 (2012).
5. Bouchoux, A., Roux-de Balmann, H. & Lutin, F. Investigation of nanofiltration as a purification step for lactic acid production processes based on conventional and bipolar electrodialysis operations. *Sep. Purif. Technol.* **52**, 266–273 (2006).
6. Do, V. T., Tang, C. Y., Reinhard, M. & Leckie, J. O. Effects of hypochlorous acid exposure on the rejection of salt, polyethylene glycols, boron and arsenic(V) by nanofiltration and reverse osmosis membranes. *Water Res.* **46**, 5217–5223 (2012).